

Image-potential states on a 2D Gr-ferromagnet hybrid: enhancing spin and stacking sensing

M. Bazarnik and A. Schlenhoff^{a)}

*Institute of Physics, University of Münster, Münster, Germany and
Department of Physics, University of Hamburg, Hamburg, Germany*

Spin-resolved scanning tunneling microscopy and spectroscopy studies of image-potential states on Gr/Fe/Ir(111) show their sensitivity to the spatial variation of the Gr-Fe distance, and of the interfacial charge and spin transfer within the moiré unit cell. A stacking contrast between fcc and hcp sites, indistinguishable in the direct tunneling mode, is provided by the image-potential states in both resonant tunneling topography and spectroscopy images. The spin-polarized measurements reveal a site- and energy-dependent spin-polarization of the image-potential states that is mapped across the moiré unit cell with a spin contrast between hcp and fcc sites unobservable in direct tunneling mode. On the on-top sites, the lowest image-potential states are found to exhibit a high spin-polarization, in contrast to the electronic states around the Fermi energy evanescent into vacuum, and attributed to their interfacial character at the respective Gr-Fe distance. Since the physisorbed graphene is only weakly spin-polarized on these sites, image-potential states reflect the spin density at buried interfaces covered by non-magnetic passivation layers. The simultaneous imaging of structural, electronic and magnetic properties, both at the surface and the buried interface will prove invaluable in research of 2D hybrids and heterostructures.

Image-potential states (IPSs) form a Rydberg-like series of unoccupied electronic states and resonances with a maximum probability density in front of the surface, vertically confined by the surface reflection properties and the collective response of the electron system that results in an attractive image charge^{1,2}. IPS properties can be studied locally utilizing scanning tunneling microscopy (STM) and spectroscopy (STS) in the field emission mode^{3,4}. Here, the electric field between the STM tip and the surface induces a Stark shift of the IPSs to higher energies potentially exceeding the local surface work function⁵. IPS wavefunctions span the entire vacuum gap between the STM tip and the sample, enabling resonant electron tunneling from the tip to the surface^{6,7}. By this means, IPSs have been used for revealing local surface properties unobtainable in the conventional direct tunneling mode of STM. Prominent examples are the atomic-scale imaging of insulating diamond⁸, the local analysis of the (spin-dependent) electron reflection at the surface^{9,10}, the identification of different metals on surfaces¹¹ or the resolution of atomic-scale spin textures at nm tip-sample-distances⁷.

With the increasing research interest in 2D materials, IPSs have regained attention¹², known as sensitive probes for interfacial coupling and charge transfer at buried interfaces¹³⁻¹⁵. For graphene (Gr)-metal hybrids, the Gr distance to the metal is decisive for the degree of its hybridization and the corresponding charge transfer, but also determines the IPS properties^{12,16-18}. With decreasing distance, the double series of IPSs of freestanding Gr evolves into quantum-well like interfacial states interacting with both surfaces at intermediate distances of about 3.7 Å, and finally, at smaller distances of about 2.2 Å,

into a single series of states that resemble those of a clean metal surface covered by a Gr spacer layer¹⁶. Deposited on a magnetic transition metal (TM), magnetism can arise in the Gr layer due to strong hybridization between Carbon π and TM d states¹⁹⁻²³. For chemisorbed Gr on Ni(111), conventional spin-polarized (SP)-STM achieved spin contrast, indicating that the electron density for states around the Fermi level E_F evanescent into vacuum is substantially spin-polarized²⁴. Likewise, an exchange-split of the first IPS has been found by nonlinear photoemission experiments²⁵. On Ni(111), Gr grows as flat layer with a small Gr-Ni separation of about 2.1 Å²⁶. In contrast, CVD grown Gr on Ir(111) exhibits a moiré superstructure resulting from the mismatch of the Gr lattice and the Ir substrate, the most commonly observed one being the R0(10x10) on (9x9)²⁷. It is characterized by three high symmetry regions where the middle of the Carbon ring is located either on-top, in an fcc or hcp position over the substrate atom. TMs like Co or Fe grow pseudomorphically on Ir(111) under Gr and, therefore, the periodicity and orientation of the moiré is preserved^{21,22,28,29}. However, while Gr interacts only weakly with Ir, hybridization with these TMs is stronger, and together with the lattice mismatch this typically leads to a pronounced buckling of the Gr layer. In case of Gr/Fe/Ir(111), the Gr-Fe distance changes from 3.6 Å on-top to 2 Å on the fcc site²⁰, thus varying between a weakly interacting and a strongly interacting system within the moiré unit cell. Notably, these distances span exactly the range where drastic changes of IPS properties are expected¹⁶.

Moreover, while in conventional STM some systems show distinct moiré with easy to distinguish high symmetry areas^{22,29}, Fe-intercalated Gr exhibits only a strong contrast between the top area and the overall rest being therefore collectively called 'valley'²¹. Conventional SP-STM has revealed significant spin-polarization of the

^{a)}Corresponding author: schlenhoff@uni-muenster.de

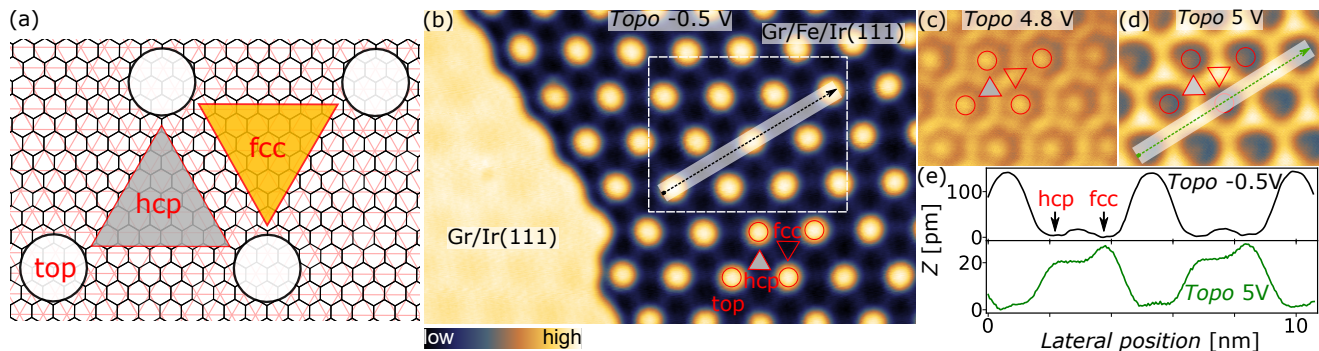


FIG. 1. **Comparison of stacking contrast in conventional and resonant tunneling topography mode.** (a) Model of Gr/Fe/Ir(111). Atoms lie at the intersections of each line. Red lines denote Fe and black lines denote carbon. Semitransparent circles mark top positions; a gray (orange) triangle denotes an hcp (fcc) region. (b) An overview conventional STM topography image recorded at $U = -0.5$ V. Regions of Gr/Ir(111) are separated from Gr/Fe/Ir(111) by a buried Ir step edge. The arrow indicates the line profile (black) shown in (e). While the corrugation within moiré is substantially reduced compared to (b), top, hcp, and fcc regions (marked in red on all panels) are discernible in (d). The arrow marks the line profile (green) depicted in (e). (e) Topography profiles for $U = -0.5$ V and $U = 5$ V, respectively, with hcp and fcc regions marked. ($I = 1$ nA).

electron density around E_F on the valley sites, while the top sites exhibit only a weak polarization^{21,22}, consistent with a spatially varying and periodic change of the magnetism in the Gr layer caused by the variation in structural geometry and hybridization within the moiré unit cell^{21,22}. To the best of our knowledge, spin-polarized IPs have been so far only studied on all-metal systems forming a single magnetic entity with a spatially uniform spin-polarization^{7,10,25,30–32}. Proven to be sensitive to the charge transfer at buried Gr-metal interfaces, the question arises how IPs do sense a respective spin transfer laterally varying within the moiré unit cell.

Here, we report on a modification of the IPs above this complex Gr-ferromagnet hybrid due to different local Gr registries within the moiré unit cell and a resulting high contrast between the fcc and hcp stacking regions in the resonant tunneling mode unachievable in conventional STM/STS. We observe a site- and energy-dependent effective spin-polarization of the IPs that can be mapped across the entire moiré unit cell. Unlike the electronic states around E_F , the lowest IPs are found to exhibit a high spin-polarization on the on-top sites attributed to their quantum-well like interfacial character at the respective Gr-Fe distance. This results in a previously unobserved increase in the spin-dependent signal when switching from direct to resonant tunneling at these sites. Moreover, mediated by the IPs, even a spin contrast between fcc and hcp sites of the moiré superstructure is observed.

Results and Discussion

The model in Fig. 1(a) presents the well-known structure of Fe-intercalated Gr on Ir(111)^{21,33}. The size of the moiré is the same as for pristine Gr/Ir(111). In a conventional STM topography image, pristine and monolayer Fe-intercalated Gr on Ir(111) can be easily distinguished by a change in corrugation of the moiré

pattern^{20,21,28,29,33} as observable in the overview image shown in Fig. 1(b). Here, pristine Gr/Ir(111) and Gr/Fe/Ir(111) are separated by a buried Ir step edge, from where the Fe intercalation has started, growing on the lower terrace²⁸. The intercalated Gr shows a starlike moiré pattern with a pronounced corrugation about five times higher compared to that of pristine Gr^{20,21,28}. The top sites are imaged as protrusions, whereas the fcc and hcp regions are separated by a small ridge of about 20 pm in height, as observable also in the line profile shown in Fig. 1(e). The apparent height difference between fcc and hcp is bias voltage dependent, but within the $[-1$ V; $+1$ V] range it is at best slightly above the noise of most modern commercial STMs leveling at ≈ 2 pm²⁰. When turning to the resonant tunneling mode, both topographies recorded at $U = 4.8$ V and 5 V shown in Fig. 1(c) and (d), respectively, exhibit an overall drop in corrugation between the top and the valley sites. This can be seen most easily by the faint contrast in Fig. 1(c), while a striking inversion of apparent corrugation is observed at $U = 5$ V. Interestingly, a contrast between fcc and hcp sites at $U = 5$ V is evident. Fig. 1(e) shows line profiles across the moiré structure measured for conventional and resonant STM, as marked in Fig. 1(b) and (d), respectively. The overall corrugation drops from 150 pm Pk-Pk at $U = -0.5$ V to just below 30 pm Pk-Pk for $U = 5$ V. At $U = 5$ V, the top sites are imaged as depressions and the ridges separating fcc and hcp turn into a plateau. Remarkably, the apparent height difference between fcc and hcp regions rises to 8 pm. In comparison to conventional STM, the combination of reduced overall roughness and large differences in apparent height in the resonant tunneling mode makes the contrast between the fcc and the hcp site distinctive.

To understand the origin of the pronounced stacking contrast observed in resonant tunneling mode, we turn

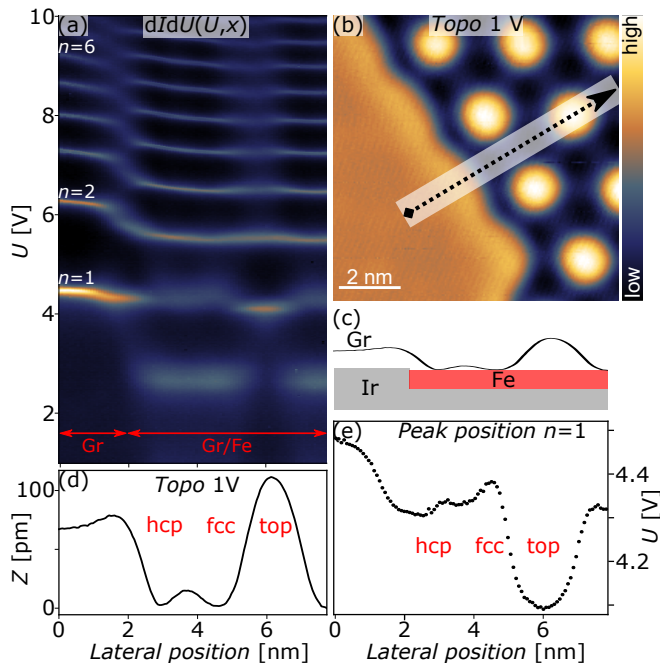


FIG. 2. Evolution of IPSSs across the lateral interface between Gr/Ir(111) and Gr/Fe/Ir(111). (a) $dI/dU(U, x)$ recorded along the line marked in (b), revealing the IPS series on Gr and Gr/Fe regions (marked on waterfall plot) and their transition ($I = 1$ nA). IPSSs of order $n = 1, 2, 6$ are labeled on the Gr site. The x -axis is shared with (d). (b) Overview conventional topography image of adjacent Gr (left) and Gr/Fe (right) regions ($U = 1$ V, $I = 5$ nA). (c) Scheme of the sample system shown in this figure. Gr covering both Ir(111) and a monolayer of Fe on Ir(111) on the lower Ir terrace. (d) Topography profile along the line marked in (b) with hcp, fcc and on-top positions marked. (e) Spatial evolution of the $n = 1$ IPSS peak position extracted by Lorentzian fits to data in (a).

to spatially-resolved investigations of IPSSs above the Fe-intercalated Gr. We start with a study of the evolution of the IPSSs across the lateral interface between Gr/Ir(111) and Gr/Fe/Ir(111). Figure 2 (a) shows a waterfall plot of the $dI/dU(U, x)$ taken along the arrow marked in the topography image shown in Fig. 2(b). The scanned surface area comprises a buried Ir step resulting in a lateral interface between the upper Ir(111) terrace and an Fe monolayer on the lower terrace both being covered by Gr, as depicted in the schematic sketch in Fig. 2(c). The corresponding topography profile along the arrow marked in Fig. 2(b) is shown in Fig. 2(d). On the pristine Gr/Ir(111) region, eight maxima can be found in the $dI/dU(U)$ curves of Fig. 2(a) revealing the lowest eight IPSSs. When going from Gr/Ir(111) to the Fe intercalated region, all IPSSs shift to lower energies, resulting in the appearance of the 9th IPSS slightly below 10 V on Gr/Fe/Ir(111). Here, the smooth spatial transition between the two IPSS series via the buried interface allows unambiguous assignment of each order n . An

additional maximum in the $dI/dU(U)$ at lower energies ($U = 2.7$ V) appears on the intercalated Gr region. Its intensity is strongest on the hcp and fcc areas, while almost diminishing on the on-top position. We attribute this feature to an interface state (IFS) originating from the hybridization of the Gr with the Fe. The occurrence of such an IFS is typical for strongly interacting Gr-metal systems^{12,14,16,18,34-36}. In Fig. 2(e) the spatial evolution of the $n = 1$ IPSS has been analyzed in more detail, showing its peak position extracted from the $dI/dU(U)$ data shown in Fig. 2(a). Following the first IPSS peak position across the intercalated moiré unit cell from hcp, via fcc, on-top to another hcp site, its energy varies between all of them. Most significantly, the IPSS for the on-top configuration exhibits the lowest energy, followed by the hcp, and fcc having the highest energy. Apparently, the IPSS's energy is sensitive to the local registry of Gr on the Fe/Ir(111).

On close inspection of the entire IPSS series it becomes evident, that even 6 nm apart from the buried step edge there is still an overall trend of shifting the peak positions to lower energies. This is attributed to a combination of edge effects and stress in Gr close to the buried step edge. Therefore, the difference in IPSS energy between the different stackings displayed in Fig. 2(d) might incorporate some additional energy shift due to the close-by interface. To circumvent that we proceed on an extended intercalated region far away from any lateral interfaces. In Fig. 3(a) $dI/dU(U)$ curves ranging from $U = 1$ V to 10 V recorded on the three high symmetry sites of the moiré unit cell of Gr/Fe/Ir(111) are shown. For comparison, a reference spectrum for the on-top position of Gr/Ir(111), recorded with the same tip, is also shown. The spectra reveal the lowest nine and seven IPSSs of the series, respectively. In addition, on the intercalated area far away from any step edge the IFS at $U = 2.7$ V is also observed. As discussed for Fig. 2(a), it is most pronounced on the hcp and fcc areas, while the on-top site of the moiré exhibits only its very weak signature. Comparing the spectra on Gr/Fe/Ir(111) to the reference spectrum on Gr/Ir(111) the IPSS series on each of the high symmetry points shifts to lower energy, as also observable in Fig. 2(a). We attribute this shift to a work function reduction of Gr/Ir(111) upon Fe intercalation. Using a simple model, as outlined in detail in the supplementary material³⁷, we find for the on-top position a reduction of the work function of Gr/Ir(111) by ≈ 0.9 eV upon intercalation of Fe. Moreover, within the Gr/Fe/Ir(111) moiré unit cell we observe variations of the work function of up to (62 ± 4) meV, the value laying well in between the lower limit given by ≈ 35 meV for the van der Waals-bound Gr/Ir(111)³⁸ and the upper limit of $(100 - 220)$ meV for strongly bound systems like Gr/Ru(0001)^{18,39} or Gr/Rh(111)^{36,40}.

Note, that the IPSS $n = 1$ on both valley sites is found at larger energies than on the top site, exhibiting an energy shift in the opposite direction to the local work function change. This "anomalous" behaviour of the first IPSS has

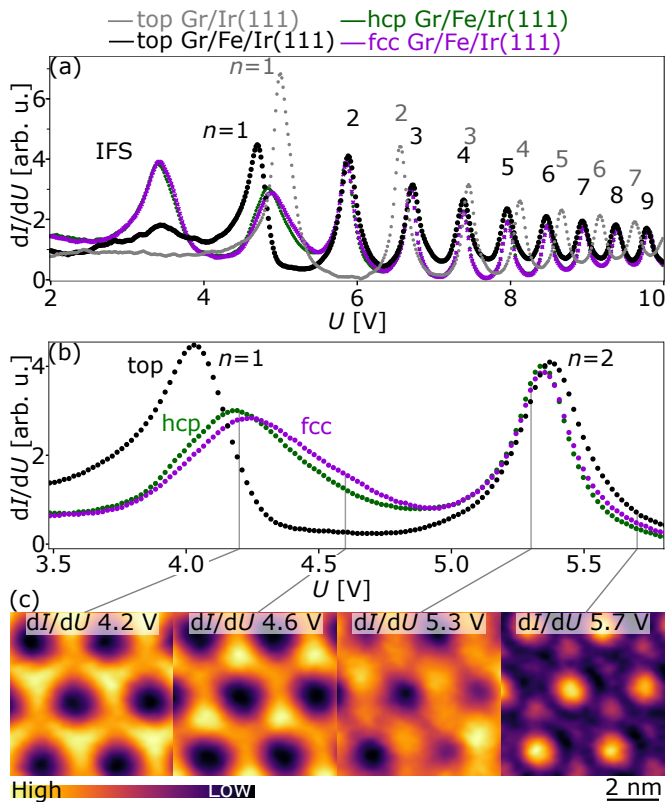


FIG. 3. **Sensing the local registry of Gr on Fe/Ir(111) by IPSSs.** (a) $dI/dU(U)$ taken on high symmetry sites of the moiré unit cell on an extended Gr/Fe/Ir(111) region (hcp in green, fcc in violet, on-top in black) and on clean Gr/Ir(111) (gray). (b) A zoom in on $n = 1$ and $n = 2$ maxima of (a) highlighting the differences between the on-top, fcc and hcp positions. (c) Series of $dI/dU(U)$ maps at indicated bias voltages exhibiting a contrast between all three high symmetry regions. ($I = 1$ nA)

been observed before on various strong interacting Gr-metal systems^{12,16–18,36,41}. It is assigned to be a consequence of the high corrugation of these systems^{16–18}: At Gr-metal distances typical for on-top sites, the IPS is expected to have a significant probability density below Gr, being thereby strongest bound to the system. In contrast, for the valley sites the Gr overlayer at smallest distance to the metal tends to push the IPS wavefunction away from the metal surface, resulting in a more delocalized (dispersive) state. This corrugation effect is expected to dominate the $n = 1$ IPS, while as n increases, the states become increasingly delocalized perpendicular to the surface and thus progressively less affected^{16,18}. In conclusion, the difference in the potential energy landscape for the IPS series on the high symmetry sites results in the observed different energetic positions of the IPSs within the moiré unit cell. The resulting change of IPS peak position and height in the $dI/dU(U)$ spectroscopy curves, as clearly observable in the zoom-in shown in Fig. 3(b), correlate with different $dI/dU(U)$ levels at a fixed bias U

on these sites. These differences can be further spatially resolved by mapping the site-dependent differential conductance $dI/dU(U, x, y)$ at fixed bias U in the resonant tunneling mode. In Fig. 3(c) exemplary $dI/dU(U)$ maps recorded on Gr/Fe/Ir(111) are shown. The respective bias U for the maps were selected to show the highest contrast between the high symmetry sites. At $U = 4.2$ V and 4.6 V the on-top sites appear dark, while the bright regions indicate the valleys with different intensities on fcc and hcp sites, respectively. Note, that when going from $U = 4.2$ V to 4.6 V, the relative intensities on the valleys change: while at $U = 4.2$ V the brightest regions in the map indicate the hcp sites, at $U = 4.6$ V the brightest regions are the fcc sites. As can be seen in Fig. 3(b), this change in intensity is related to the small shift of the IPS peak position between hcp and fcc sites. The observed differences in the local differential conductance are also responsible for the stacking contrast observed in the topography images shown in Fig. 1, since in topography images recorded at a given bias voltage U all tunneling channels are integrated from E_F up to an energy defined by eU . Notably, the stacking contrast in the dI/dU maps and its inversion are also observable for the $n = 2$ IPS as exemplary shown in Fig. 3(c) for maps recorded at $U = 5.3$ V and 5.7 V.

In order to investigate the spin polarization of IPSSs above the Gr-ferromagnet hybrid, we performed spin-resolved STS in the resonant tunneling mode on the fcc, hcp and on-top areas with parallel and antiparallel alignment of the tip and sample magnetization by means of external magnetic fields of $B = \pm 1$ T, respectively. The respective spin-resolved $dI/dU(U)$ curves covering the energy range from 1 eV via the IFS up to the 5th IPS are shown in Fig. 4(a). Clearly, on each high symmetry site of the moiré unit cell the spin-dependent curves for the two magnetic configurations differ, indicating a spin-polarization of the IFS and the IPS series^{30,31}. On the fcc position, for the peaks in $dI/dU(U)$ corresponding to the $n = 1$ IPS we find an effective spin-splitting of (15 ± 3) meV. For the on-top position, the first IPS related peak is spin-split by even (21 ± 3) meV. These values are comparable to the effective spin-splitting of IPSSs observed by resonant SP-STs on thin-film metals on heavy-element substrates^{30,31}. The calculated asymmetry of the spin-dependent $dI/dU(U)$ curves for each site is plotted in the lower panel of Fig. 4(a). It is a measure for the effective electron spin-polarization at the respective energy eU . Obviously, the electron spin-polarization is strongly energy-dependent determined by the presence and energetic positions of the IFS and IPSSs. Moreover, a considerable spatial variation within the moiré unit cell is observed.

Focusing first on the valley sites, in Fig. 4(a) we find for both sites five broad maxima in the asymmetry curve corresponding to the IFS and the first four IPSSs, respectively. Compared to the corresponding peaks in the respective $dI/dU(U)$ curves these maxima are shifted to higher energies caused by a slightly different shape of

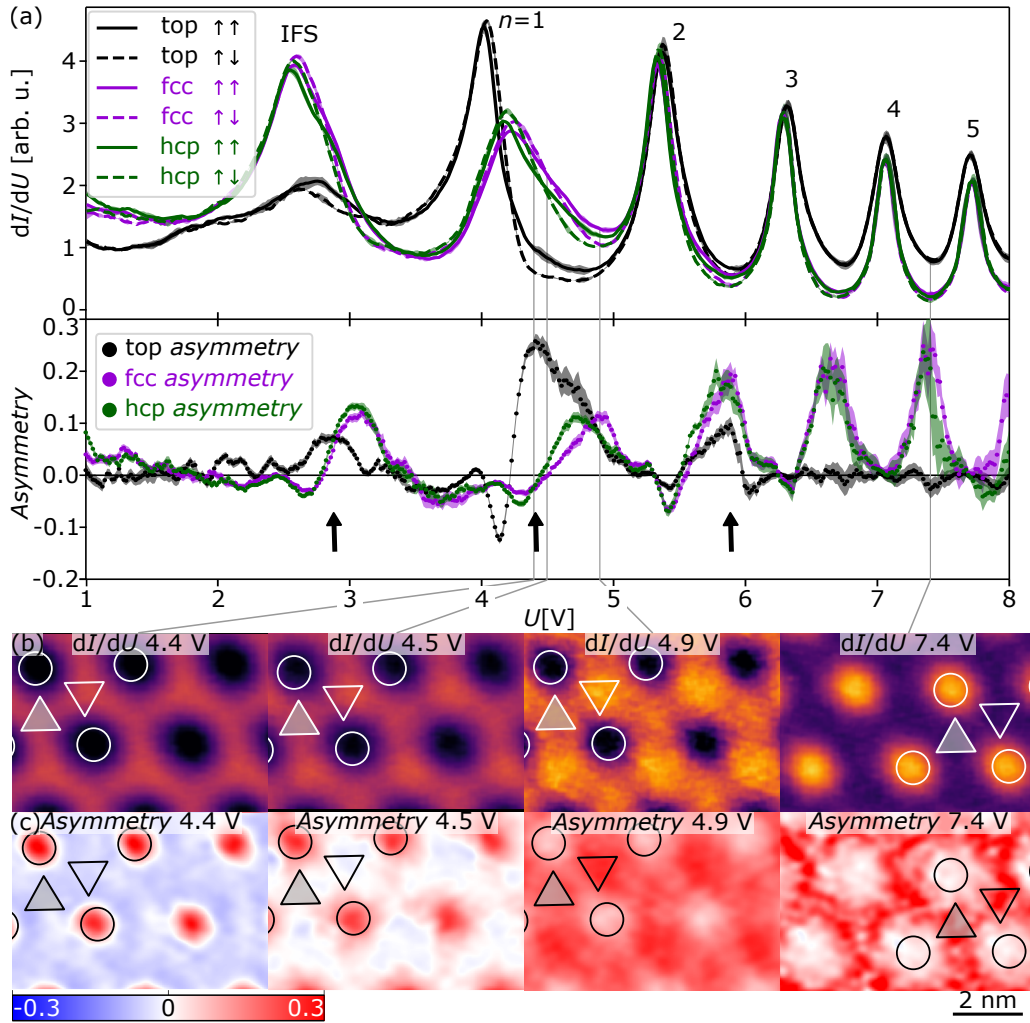


FIG. 4. **Spin contrast within the Gr/Fe/Ir(111) moiré unit cell mediated by IPSS.** (a) **Top:** Spin-polarized tunneling spectra $dI/dU(U)$ recorded with an Fe-coated W tip for on-top, fcc and hcp sites in an external magnetic field of $B = \pm 1$ T along the tip, respectively. The two configurations of magnetic moments of tip and sample measured are marked with solid and dashed lines. Six peaks in each curve are observed, related to IFS and the lowest five IPSS. **Bottom:** Asymmetry plots computed from the above spectra. For the on-top site, three broad maxima (marked by arrows) related to the IFS and the first two IPSS are observable. For the fcc (hcp) site, five broad maxima are found at $U = 3.11$ V, 4.9 V, 5.9 V, 6.64 V and 7.39 V ($U = 3.07$ V, 4.7 V, 5.8 V, 6.60 V and 7.35 V) related to the IFS and the lowest four IPSS, respectively. (b) dI/dU maps at indicated bias voltages recorded for the parallel alignment of tip and sample magnetic moments. (c) Corresponding asymmetry maps computed from dI/dU maps registered in the parallel and antiparallel configurations of tip and sample magnetic moments. The voltages at which the maps were recorded are marked in (a) by grey lines. The moiré unit cell is depicted on all maps. ($I = 1$ nA).

the $dI/dU(U)$ curves for the two magnetic configurations and the overlap of falling and rising flanks of neighbouring peaks in the respective $dI/dU(U)$ curves. With an asymmetry of $> 10\%$ for both, the IFS and the $n = 1$ IPS on the valleys exhibit a spin-polarization of same magnitude, proving their strong hybridization. Note, that we expect a considerable spatial overlap of the IPS wavefunction with the IFS. The latter has a significant weight of its probability density above the Gr as proven by its pronounced signature in our STS data, and in analogy to a previous study for Gr-Ru¹⁸. In the measured bias

range, spin asymmetry reaches 25% at close to 7.4 V. However, at these high voltages the signal to noise ratio gets worse as well. Conventional SP-STs in a bias range of $[-1$ V; $+1$ V] on the same sample with the same probe tip reveals an asymmetry of up to 42% on both valley sites⁴², consistent with previous studies^{20,21} and attributed to the strong Gr-Fe hybridization on these sites. Consequently, we observe a reduction of the spin-dependent signal by up to 76% when changing from the direct to the resonant tunneling mode. Such a strong decrease in the magnetic signal yet appeared to be typ-

ical when changing to spin-polarized resonant tunneling through IPSs, as this trend has been observed on all the previously studied systems^{7,10,30,31}.

Interestingly, we observe a completely different behaviour for the on-top sites of this complex Gr/Fe/Ir system. First, we observe three broad maxima in the respective asymmetry curve marked by arrows in Fig. 4(a) related to the IFS and the first two IPSs. For energies larger than 6.2 eV the spin asymmetry is within the noise level, indicating a strongly reduced spin-polarization of the higher-order IPSs on the on-top sites. Second, our conventional SP-STs measurements of states around E_F exhibit an only weak spin-polarization of the on-top sites with an asymmetry of $\leq 10\%$ reflecting the physisorbed character of Gr on Fe/Ir(111) on this position⁴², as previously studied^{20,21}. Surprisingly, we find a large asymmetry of $(26 \pm 1)\%$ at $U = 4.4$ V, corresponding to the falling flank of the $n = 1$ IPS peak in $dI/dU(U)$, and still a considerable value of $(9 \pm 2)\%$ in between the spectroscopic peaks of the second and third IPS. Consequently, we observe for the first time a higher spin-polarization of an IPS compared to the states around E_F , and accordingly an increase in the spin-dependent signal when turning to the resonant tunneling mode. From previous theoretical and experimental work it is known, that because of the physisorbed character of Gr in the local on-top registry, the largest spin-density is concentrated in the Fe layer below the Gr²⁰. Naturally, conventional SP-STs is most sensitive to the evanescent tail of spin-polarized states localized in the very top-most layer. In contrast, resonant SP-STs detects IPSs in front of the surface, which, due to their different nature and ability to penetrate the sub-surface region, may reflect not only charge accumulation but also spin accumulation at buried interfaces, as demonstrated here. Consequently, our observations indicate a significant penetration of the first two IPSs into the Gr/Fe/Ir(111) and a spin-dependent scattering at the buried Fe layer.

Moreover, while the fcc and hcp areas are indistinguishable in the low bias spin asymmetry^{20,21,42}, in resonant SP-STs we observe fine differences in the effective spin polarization between those different valley sites. In Fig. 4(a), a considerable difference in the spin asymmetry for the respective sites is found between the $n = 1$ and $n = 2$ IPS related $dI/dU(U)$ peaks. Here hcp exhibits a higher spin polarization at a bias of $U = 4.7$ V, while the fcc spin polarization dominates at $U = 4.9$ V. Evidently, the spin contrast between the high-symmetry sites in resonant SP-STs at a fixed bias voltage arise from the site-dependent slightly different energetic positions of the spin-polarized IPSs. In order to map the effective IPSs' spin-polarization across the moiré unit cell, dI/dU maps on the very same area have been recorded in the resonant tunneling mode once for parallel and once for antiparallel alignment of tip and sample magnetization and the corresponding asymmetry maps were deduced. Fig. 4(b) shows four exemplary dI/dU maps recorded at different bias voltages, as marked in Fig. 4(a). The cor-

responding spin asymmetry maps are shown in Fig. 4(c). At $U = 4.4$ V we observe the highest electron spin polarization on the on-top position and a sing inversion between the on-top and the valley sites. Such a sing inversion has been previously observed also for states around E_F ^{21,22,42}. However, the asymmetry map at $U = 4.5$ V exhibits the most pronounced spin contrast between the fcc and hcp positions. Here, the asymmetry for hcp has a positive sign while for fcc it is negative. At the same time the on-top sites exhibit a very strong positive spin polarization. At $U = 4.9$ V all three regions exhibit a positive electron spin polarization in the asymmetry map. However, as also evident from the spectroscopy shown in Fig. 4(a), the spin asymmetry for on-top and hcp site is lower than for the fcc, while for the latter it is the highest in the energy range between $n = 1$ and $n = 2$. Finally, we demonstrate spatial mapping of the high energy electron spin polarization, as shown by the exemplary asymmetry map at $U = 7.4$ V in Fig. 4(c). As discussed before, the effective spin polarization on the on-top positions is negligible while it is positive for fcc and hcp in accordance with the asymmetry curves shown in Fig. 4(a). Here, the increased noise level hides the contrast in the asymmetry maps between the two valley regions being expected from the spectroscopy curves. However, our experiments demonstrate a site- and energy-dependent effective spin-polarization of the IPSs on the Gr-ferromagnet hybrid that can be mapped across the entire moiré unit cell.

Conclusions

We were able to show a contrast in high-bias resonant tunneling images and spectroscopy between fcc and hcp stacking sites of the moiré unit cell in a Gr-based 2D hybrid system, unachievable in conventional low bias STM. The contrast originates from the spatial variation of the IPSs, being sensitive to the local surface work function variation within the moiré unit cell, determined to be in the order of (62 ± 4) meV, as well as to the strong Gr-Fe distance variation. The spin-polarized measurements reveal a site- and energy-dependent effective IPSs' spin-polarization, providing a spin contrast between hcp and fcc sites unobtained in conventional SP-STM/STS. Moreover, the first two IPSs exhibit a huge spin-polarization on the top-sites, where the physisorbed Gr is known to exhibit only a weak spin-polarization. This finding implies a significant probability density of these IPSs below the Gr, sensing the spin-density in the buried Fe layer. Consequently, our work demonstrates that the lowest order IPSs can be used to locally sense the spin density at magnetic interfaces buried by a non-magnetic passivation layer. In light of the rising field of twistrionics where the interface of stacked 2D systems and the interplay of charge, spin and moiré superlattice structure is decisive for emerging phenomena, atomic-scale investigations of IPSs may provide further insight into these buried processes.

Methods

All experiments were performed in an UHV system equipped with a low temperature SP-STM and two

preparation chambers for substrate cleaning, Gr CVD growth, and metal deposition⁴³. The Ir(111) single crystal was cleaned by repeated cycles of Ar⁺ sputtering (800 V, 5E–6 mbar), annealing at temperatures ranging from $T = 900$ K to 1500 K in the presence of O₂ and a flash annealing at $T \approx 1500$ K. The Gr layer was grown in situ on Ir(111) by thermal decomposition of ethylene molecules following the procedure described in ref.²⁷. Less than monolayer Fe intercalation was achieved in situ following the procedure of ref.²⁸. After preparation samples were transferred in vacuo to the SP-STM setup and cooled down to the measurement temperature of $T = 6.5$ K. A lock-in detection technique was used to obtain dI/dU maps and point spectroscopy data adding a small AC modulation $U_{Pk-Pk} = 50$ mV to the bias voltage U at $f = 1111.1$ Hz. The dI/dU maps were recorded simultaneously with the STM topography in the constant-current mode. High bias differential conductance spectra have been recorded while maintaining a constant current setpoint during the bias voltage sweep up to $U = 10$ V^{3,4,7}. IPS position in point spectra was extracted by fitting Lorentzian function to each peak. The work function was determined by fitting to $n = < 3, 6 >$. Electrochemically etched tungsten tips cleaned by standard in vacuo flash annealing at $T \approx 2500$ K and coated with ~ 50 atomic layers of Fe were used as probes for our SP-STM studies. These Fe/W tips are soft ferromagnets and can be easily aligned with an external magnetic field. The sample is a hard magnet with an out-of-plane easy axis and coherisive field around 6 T^{20,21,33}. Therefore, applying fields along the axis of the tip with strengths up to 2 T we can easily control the alignment of the magnetic moment of the tip while not changing the alignment of magnetic moments on the sample. The spin asymmetry is defined here as $\text{Asymmetry} = (dI/dU \uparrow\uparrow - dI/dU \uparrow\downarrow) / (dI/dU \uparrow\uparrow + dI/dU \uparrow\downarrow)$ where the arrow directions refer to the magnetization direction of the SP-STM probe tip and the sample. The error bar shown in Fig. 4(a) is determined from a control experiment in which the tip magnetization has been flipped back to its initial state and an asymmetry of both the first $dI/dU \uparrow\uparrow$ and last $dI/dU \uparrow\uparrow$ measurements was computed. All data has been processed using self-written python code and Gwyddion⁴⁴ software.

ACKNOWLEDGMENTS

The authors would like to thank professor R. Wiesendanger for support and provision of laboratories and infrastructure.

- ¹P. M. Echenique and J. B. Pendry, *J. Phys. C: Solid State Phys.* **11**, 2065 (1978).
- ²U. Höfer and P. M. Echenique, *Surface Science Present challenges in surface science, a special issue in honour of Dietrich Menzel*, **643**, 203 (2016).
- ³G. Binnig, K. H. Frank, H. Fuchs, N. Garcia, B. Reihl, H. Rohrer, F. Salvan, and A. R. Williams, *Phys. Rev. Lett.* **55**, 991 (1985).

- ⁴R. S. Becker, J. A. Golovchenko, and B. S. Swartzentruber, *Phys. Rev. Lett.* **55**, 987 (1985).
- ⁵S. Crampin, *Phys. Rev. Lett.* **95**, 046801 (2005).
- ⁶K. H. Gundlach, *Solid-State Electronics* **9**, 949 (1966).
- ⁷A. Schlenhoff, S. Kovarik, S. Krause, and R. Wiesendanger, *Applied Physics Letters* **116**, 122406 (2020).
- ⁸K. Bobrov, A. J. Mayne, and G. Dujardin, *Nature* **413**, 616 (2001).
- ⁹A. J. Caamaño, Y. Pogorelov, O. Custance, J. Méndez, A. M. Baró, J. Y. Veullen, J. M. Gomez-Rodriguez, and J. J. Sáenz, *Surface Science* **426**, L420 (1999).
- ¹⁰A. Schlenhoff, S. Kovarik, S. Krause, and R. Wiesendanger, *Phys. Rev. Lett.* **123**, 087202 (2019).
- ¹¹T. Jung, Y. W. Mo, and F. J. Himpsel, *Phys. Rev. Lett.* **74**, 1641 (1995).
- ¹²B. Borca and H. J. W. Zandvliet, *Applied Materials Today* **39**, 102304 (2024).
- ¹³D. Niesner and T. Fauster, *J. Phys.: Condens. Matter* **26**, 393001 (2014).
- ¹⁴S. Bose, V. M. Silkin, R. Ohmann, I. Brihuega, L. Vitali, C. H. Michaelis, P. Mallet, J. Y. Veullen, M. A. Schneider, E. V. Chulkov, P. M. Echenique, and K. Kern, *New J. Phys.* **12**, 023028 (2010).
- ¹⁵X. Liu, L. Wang, B. I. Yakobson, and M. C. Hersam, *Nano Lett.* **21**, 1169 (2021).
- ¹⁶N. Armbrust, J. Güdde, and U. Höfer, *New J. Phys.* **17**, 103043 (2015).
- ¹⁷N. Armbrust, J. Güdde, P. Jakob, and U. Höfer, *Phys. Rev. Lett.* **108**, 056801 (2012).
- ¹⁸B. Borca, S. Barja, M. Garnica, D. Sánchez-Portal, V. M. Silkin, E. V. Chulkov, C. F. Hermanns, J. J. Hinarejos, A. L. Vázquez de Parga, A. Arnau, P. M. Echenique, and R. Miranda, *Phys. Rev. Lett.* **105**, 036804 (2010).
- ¹⁹M. Weser, Y. Rehder, K. Horn, M. Sicot, M. Fonin, A. B. Preobrajenski, E. N. Voloshina, E. Goering, and Y. S. Dedkov, *Applied Physics Letters* **96**, 012504 (2010).
- ²⁰J. Brede, N. Atodiresei, V. Caciuc, M. Bazarnik, A. Al-Zubi, S. Blügel, and R. Wiesendanger, *Nature Nanotech* **9**, 1018 (2014).
- ²¹R. Decker, M. Bazarnik, N. Atodiresei, V. Caciuc, S. Blügel, and R. Wiesendanger, *J. Phys.: Condens. Matter* **26**, 394004 (2014).
- ²²R. Decker, J. Brede, N. Atodiresei, V. Caciuc, S. Blügel, and R. Wiesendanger, *Phys. Rev. B* **87**, 041403 (2013).
- ²³H. Vita, S. Böttcher, P. Leicht, K. Horn, A. B. Shick, and F. Mácá, *Phys. Rev. B* **90**, 165432 (2014).
- ²⁴L. Dzemiantsova, M. Karolak, F. Lofink, A. Kubetzka, B. Sachs, K. von Bergmann, S. Hankemeier, T. Wehling, R. Frömter, H. Oepen, A. Lichtenstein, and R. Wiesendanger, *Phys. Rev. B* **84**, 205431 (2011).
- ²⁵S. Achilli, S. Tognolini, E. Fava, S. Ponzoni, G. Drera, C. Cepek, L. L. Patera, C. Africh, E. D. Castillo, M. I. Trioni, and S. Pagliara, *New J. Phys.* **20**, 103039 (2018).
- ²⁶E. Voloshina and Y. Dedkov, *Phys. Chem. Chem. Phys.* **14**, 13502 (2012).
- ²⁷A. T. N'Diaye, J. Coraux, T. N. Plasa, C. Busse, and T. Michely, *New J. Phys.* **10**, 043033 (2008).
- ²⁸M. Bazarnik, R. Decker, J. Brede, and R. Wiesendanger, *Surface Science* **639**, 70 (2015).
- ²⁹M. Bazarnik, J. Brede, R. Decker, and R. Wiesendanger, *ACS Nano* **7**, 11341 (2013).
- ³⁰A. Schlenhoff, S. Krause, A. Sonntag, and R. Wiesendanger, *Phys. Rev. Lett.* **109**, 097602 (2012).
- ³¹A. Kubetzka, M. Bode, and R. Wiesendanger, *Applied Physics Letters* **91**, 012508 (2007).
- ³²M. Donath, C. Math, M. Pickel, A. B. Schmidt, and M. Weinelt, *Surface Science Wagga Symposium on Surfaces and Interfaces - 2006*, **601**, 5701 (2007).
- ³³E. Sierda, M. Elsebach, R. Wiesendanger, and M. Bazarnik, *Nano Lett.* **19**, 9013 (2019).
- ³⁴A. Garcia-Lekue, T. Balashov, M. Olle, G. Ceballos, A. Arnau, P. Gambardella, D. Sanchez-Portal, and A. Mugarza, *Phys. Rev.*

- Lett. **112**, 066802 (2014).
- ³⁵M. Gyamfi, T. Eelbo, M. Waśniowska, and R. Wiesendanger, Phys. Rev. B **85**, 205434 (2012).
- ³⁶B. Wang, M. Caffio, C. Bromley, H. Früchtel, and R. Schaub, ACS Nano **4**, 5773 (2010).
- ³⁷See the Supplemental Material for the determination of the local work functions for Gr/Ir(111) and Gr/Fe/Ir(111).
- ³⁸Y. Dedkov and E. Voloshina, Phys. Chem. Chem. Phys. **16**, 3894 (2014).
- ³⁹T. Brugger, S. Günther, B. Wang, J. H. Dil, M.-L. Bocquet, J. Osterwalder, J. Wintterlin, and T. Greber, Phys. Rev. B **79**, 045407 (2009).
- ⁴⁰H. G. Zhang, H. Hu, Y. Pan, J. H. Mao, M. Gao, H. M. Guo, S. X. Du, T. Greber, and H.-J. Gao, J. Phys.: Condens. Matter **22**, 302001 (2010).
- ⁴¹V. Carnevali, A. Sala, P. Biasin, M. Panighel, G. Comelli, M. Persi, and C. Africh, Carbon **210**, 118055 (2023).
- ⁴²See Supplemental Material for spin-resolved $dI/dU(U)$ curves in a bias voltage range of $[-1V;+1V]$ recorded in parallel and antiparallel alignment of tip and sample magnetization, respectively, and corresponding asymmetry curves for the different high symmetry sites within the moiré unit cell.
- ⁴³C. Wittneven, R. Dombrowski, S. H. Pan, and R. Wiesendanger, Review of Scientific Instruments **68**, 3806 (1997).
- ⁴⁴D. Nečas and P. Klapetek, centr.eur.j.phys. **10**, 181 (2012).

Image potential states on a 2D Gr-ferromagnet hybrid: enhancing spin and stacking sensing - Supplementary Materials

M. Bazarnik^{1,2} and A. Schlenhoff^{1,2,*}

¹*Institute of Physics, University of Münster, Münster, Germany*

²*Department of Physics, University of Hamburg, Hamburg, Germany*

Determination of local work functions for Gr/Ir(111) and Gr/Fe/Ir(111)

Comparing the $dI/dU(U)$ spectra on Gr/Fe/Ir(111) to the reference spectrum on Gr/Ir(111), shown in Fig. 3(a) in the main manuscript, the IPS series on each of the high symmetry points shifts to lower energy. We attribute this shift to a work function reduction of Gr/Ir(111) upon Fe intercalation. This can be further analysed using a simple model. Assuming an homogeneous electric field in front of the surface for the IPSs of order $n = [3; 7]$ observed in constant current spectroscopy, their energetic positions U_n can be approximated by a linear function of $(n - 0.25)^{2/3}$, with the y-intercept yielding a rough value for the surface work function [1]. In Fig. 1 the respective plots and fit curves for the three different high symmetry sites on Gr/Fe/Ir(111) as well as for Gr/Ir(111) are shown. For the on-top position of the pristine Gr/Ir(111) we find $\phi_{\text{Gr/Ir}}^{\text{top}} = (4.364 \pm 0.003)$ eV, which is slightly lower than the (4.65 ± 0.1) eV obtained by two-photon photoemission [2] and the 4.422 eV obtained by DFT calculations [3]. However, when going to the respective on-top position of the Fe-intercalated region a considerable lowering of the work function by ≈ 0.9 eV is evident in the data shown in Fig. 1, yielding $\phi_{\text{Gr/Fe/Ir}}^{\text{top}} = (3.447 \pm 0.003)$ eV and indicating a considerable charge transfer from Fe towards Gr. While this has not been studied before, upon intercalation of Cobalt resulting in a similar system a comparable decrease of the work function to about 3.3 eV has been reported [4]. Furthermore, within the Gr/Fe/Ir(111) moiré unit cell we observe variations of the work function of up to (62 ± 4) meV. Compared to the value on the top site, the work function for the fcc site is lower ($\phi_{\text{Gr/Fe/Ir}}^{\text{fcc}} = (3.391 \pm 0.003)$ eV) and the lowest for the hcp site ($\phi_{\text{Gr/Fe/Ir}}^{\text{hcp}} = (3.385 \pm 0.003)$ eV), in agreement with a strong hybridization of Gr with Fe/Ir(111)

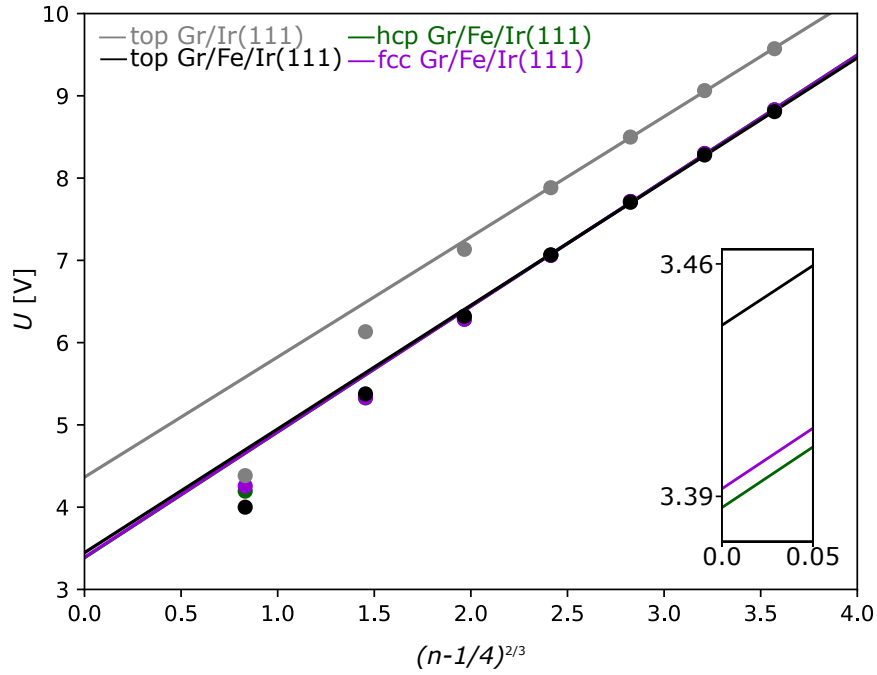


FIG. 1. **Work function determination.** IPS energy U_n as a function of $(n - 1/4)^{2/3}$ and line fits used to determine the local work function. (Peak positions U_n are deduced from the $dI/dU(U)$ spectra taken on high symmetry sites of the moiré unit cell on Gr/Fe/Ir(111) (hcp in green, fcc in violet, on-top in black) and on clean Gr/Ir(111) (gray), presented in Fig. 3a of the main manuscript.) **Inset:** A zoom on the y-intercepts of the lines, yielding the work function values for the intercalated region.

on these valley sites and the smallest Gr-Fe-distance on the hcp site [5, 6]. The observed work function variation within the moiré unit cell lies well in between the lower limit given by about 35 meV for the van der Waals-bound Gr/Ir(111) [3] and the upper limit of (100 – 220) meV for strongly covalently bound systems like Gr/Ru(0001) [7, 8] or Gr/Rh(111) [9, 10].

Reference SP-STs study of electronic states around the Fermi level

We recorded spin-polarized constant height tunneling spectra $dI/dU(U)$ between $U = -1$ V and $+1$ V taken on the exact same sites, respectively, as for the spin-polarized high-bias resonant tunneling spectra $dI/dU(U)$ presented in Fig. 4(a) in the main manuscript. In order to exclude any tip-related artifacts, we used the exact same tip. The spectra were registered in parallel and antiparallel configurations of magnetic moments alignment between the tip and the sample and a corresponding spin asymmetry was computed. A broad state with a maximum at $U = -0.175$ V is present in parallel magnetic moment configuration of tip and sample in all three configurations. This state is highly spin-polarized for hcp and fcc positions and therefore diminishes in the antiparallel configuration. In line with previously reported data [5, 11], the highest spin polarization is visible between $U = -0.2$ V and -0.3 V. Both of the valley sites reach a 42% spin asymmetry and within the noise level are indistinguishable, while the on-top site has a circa 10% spin polarization. Note the change of sign between the valley sites and the on-top position at $U = -0.5$ V.

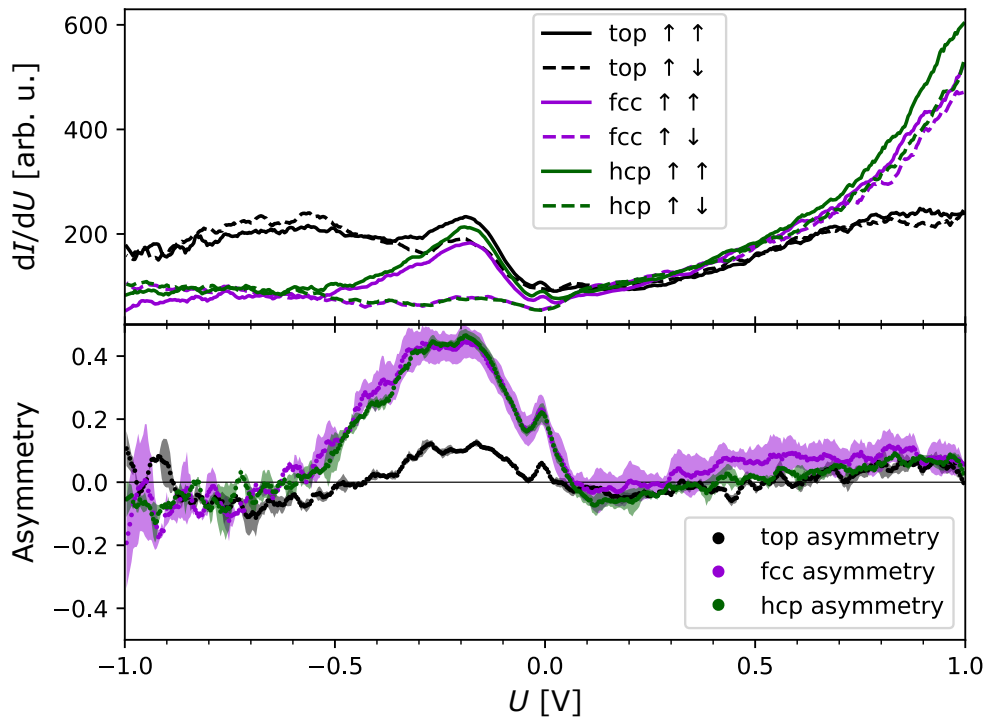


FIG. 2. **Spin polarization near Fermi energy.** **Top:** Spin-polarized constant height tunneling spectra $dI/dU(U)$ registered with an Fe-coated W tip for on-top, fcc and hcp positions in external magnetic fields of ± 1 T along the tip, respectively. Two configurations of magnetic moments of sample and tip measured are marked with solid and dashed lines. **Bottom:** Asymmetry plot computed from the above spectra. The error bar comes from a control experiment in which the tip magnetization was flipped to its original state and an asymmetry of both the first and last measurements was computed. Stabilization parameters: $U = 1$ V, $I_t = 4.5$ nA.

* Corresponding author: schlenhoff@uni-muenster.de

- [1] A. Schlenhoff, G. C. Kokkorakis, and J. P. Xanthakis, *Applied Physics Letters* **120**, 261601 (2022).
- [2] D. Niesner, T. Fauster, J. I. Dadap, N. Zaki, K. R. Knox, P.-C. Yeh, R. Bhandari, R. M. Osgood, M. Petrović, and M. Kralj, *Phys. Rev. B* **85**, 081402 (2012).
- [3] Y. Dedkov and E. Voloshina, *Phys. Chem. Chem. Phys.* **16**, 3894 (2014).
- [4] A. Calloni, G. Bussetti, G. Avvisati, M. S. Jagadeesh, D. Pacilè, A. Ferretti, D. Varsano, C. Cardoso, L. Duò, F. Ciccacci, and M. G. Betti, *The Journal of Chemical Physics* **153**, 214703 (2020).
- [5] R. Decker, M. Bazarnik, N. Atodiresei, V. Caciuc, S. Blügel, and R. Wiesendanger, *J. Phys.: Condens. Matter* **26**, 394004 (2014).
- [6] J. Brede, N. Atodiresei, V. Caciuc, M. Bazarnik, A. Al-Zubi, S. Blügel, and R. Wiesendanger, *Nature Nanotech* **9**, 1018 (2014).
- [7] B. Borca, S. Barja, M. Garnica, D. Sánchez-Portal, V. M. Silkin, E. V. Chulkov, C. F. Hermanns, J. J. Hinarejos, A. L. Vázquez de Parga, A. Arnau, P. M. Echenique, and R. Miranda, *Phys. Rev. Lett.* **105**, 036804 (2010).
- [8] T. Brugger, S. Günther, B. Wang, J. H. Dil, M.-L. Bocquet, J. Osterwalder, J. Wintterlin, and T. Greber, *Phys. Rev. B* **79**, 045407 (2009).
- [9] H. G. Zhang, H. Hu, Y. Pan, J. H. Mao, M. Gao, H. M. Guo, S. X. Du, T. Greber, and H.-J. Gao, *J. Phys.: Condens. Matter* **22**, 302001 (2010).
- [10] B. Wang, M. Caffio, C. Bromley, H. Früchtl, and R. Schaub, *ACS Nano* **4**, 5773 (2010).
- [11] E. Sierda, M. Elsebach, R. Wiesendanger, and M. Bazarnik, *Nano Lett.* **19**, 9013 (2019).